AGU100 ADVANCING EARTH AND SPACE SCIENCE

Water Resources Research

RESEARCH ARTICLE
10.1029/2018WR022972

Key Points:
- Existing traditional methods for predicting seawater intrusion in coastal boreholes are inadequate
- Recent data suggest that borehole self-potentials respond to an approaching saline front several days in advance of breakthrough
- A numerical model of self-potentials suggests that the precursor is a response to seawater filling fractures near the base of the borehole

Supporting Information:
- Supporting Information S1

Correspondence to:
M. T. Graham,
m.graham14@imperial.ac.uk

Citation:
Graham, M. T., MacAllister, DJ., Vinogradov, J., Jackson, M. D., & Butler, A. P. (2018). Self-potential as a predictor of seawater intrusion in coastal groundwater boreholes. *Water Resources Research*, *54*, 6055–6071. https://doi.org/10.1029/2018WR022972

Received 19 MAR 2018
Accepted 30 JUN 2018
Accepted article online 7 JUL 2018
Published online 6 SEP 2018

Self-Potential as a Predictor of Seawater Intrusion in Coastal Groundwater Boreholes

M. T. Graham[1,2], DJ. MacAllister[1,2,3], J. Vinogradov[2,4], M. D. Jackson[2], and A. P. Butler[1]

[1]Department of Civil and Environmental Engineering, Imperial College London, London, UK, [2]Department of Earth Science and Engineering, Imperial College London, London, UK, [3]Now at British Geological Survey, The Lyell Centre, Edinburgh, UK, [4]Now at School of Engineering, King's College, University of Aberdeen, Aberdeen, UK

Abstract Monitoring of self-potentials (SPs) in the Chalk of England has shown that a consistent electrical potential gradient exists within a coastal groundwater borehole previously affected by seawater intrusion (SI) and that this gradient is absent in boreholes further inland. Furthermore, a small but characteristic reduction in this gradient was observed several days prior to SI occurring. We present results from a combined hydrodynamic and electrodynamic model, which matches the observed phenomena for the first time and sheds light on the source mechanisms for the spatial and temporal distribution of SP. The model predictions are highly sensitive to the relative contribution of electrochemical exclusion and diffusion potentials, the *exclusion efficiency*, in different rock strata. Geoelectric heterogeneity, largely due to marls and hardgrounds with a relatively high exclusion efficiency, was the key factor in controlling the magnitude of the modeled SP gradient ahead of the saline front and its evolution prior to breakthrough. The model results suggest that, where sufficient geoelectric heterogeneity exists, borehole SP may be used as an early warning mechanism for SI.

1. Introduction

Globally, groundwater provides the main source of water for human consumption and is critically important for agriculture in many countries (WWAP, 2014). Groundwater demand is particularly high in coastal areas, where population density is more than three times the global average (Small & Nicholls, 2003).

Many coastal aquifers are vulnerable to seawater intrusion (SI), with numerous incidences reported in every inhabited continent (Barlow & Reichard, 2010; Bocanegra et al., 2010; Custodio, 2010; Morgan & Werner, 2015; Shi & Jiao, 2014; Steyl & Dennis, 2010). SI risks are greatest when the water table is low relative to local sea levels, a situation exacerbated by increasing abstractions and climatic variability.

Traditional approaches for characterizing SI fall into three main categories (Werner et al., 2013): borehole hydrochemistry, monitoring of groundwater levels, and geophysical investigations. Monitoring of borehole water levels and hydrochemistry often fails to predict the timing of SI, particularly in heterogeneous aquifers, where seawater may be transported along a small number of preferential flow paths. Time-lapse resistivity and electromagnetic surveys have been used in various studies to investigate SI (e.g., Comte & Banton, 2007; Fitterman, 2014; McDonald et al., 1998), although these typically require a large footprint for the long-term installation of monitoring apparatus or repeated surveys during the predicted period of SI risk.

This paper explores whether borehole measurements of self-potential (SP) may represent an alternative means of identifying a nearby saline front, as concentration gradients are known to generate SP, through the development of an electrochemical exclusion-diffusion potential V_{EED} (e.g., Jackson, 2015; Jouniaux et al., 2009; Lanteri et al., 2009; Leinov & Jackson, 2014; Martínez-Pagán et al., 2010; Revil, 1999; Westermann-Clark & Christoforou, 1986). The relatively low cost of monitoring equipment, combined with a small footprint within a single borehole, represent significant advantages compared to traditional methods for identifying SI.

Electrochemically induced SPs have been used to track the position of an injected saline front in both field (Jougnot et al., 2015; Sandberg et al., 2002) and laboratory (Martínez-Pagán et al., 2010) experiments, with the latter suggesting that an SP signal occurs ahead of any increase in salinity. These experimental findings are supported by numerical modeling of SI in hydrocarbon reservoirs, where changes in SP occurred several tens of meters ahead of the saline front (Gulamali et al., 2011; Jackson et al., 2012).

MacAllister et al. (2016) was the first study to demonstrate a link between tidal processes and borehole SP in a coastal aquifer. This was done by monitoring borehole SP and fluid electrical conductivity σ_f in a coastal borehole in the UK Chalk subject to regular SI (the Saltdean Observation Borehole, OBH). MacAllister et al. (2018) then demonstrated that the tidal SP signal in the Saltdean OBH was dominated by the electrochemically induced component of SP across a remote saline front.

MacAllister et al. (2018) also showed that the Saltdean OBH displays a consistent SP gradient ahead of the saline front and that this feature is absent in Chalk boreholes further inland. Moreover, a characteristic reduction in this gradient, or precursor, occurs several days prior to saline breakthrough in the borehole (MacAllister, 2016). Numerical modeling conducted by MacAllister (2016) and MacAllister et al. (2018) was unable to replicate the magnitude of the initial SP gradient and did not attempt to simulate the subsequent precursor. Consequently, the source mechanisms for these phenomena remain unexplained.

The aims of the present study are twofold. First, we aim to match the observed SP gradient within the borehole using a combined hydrodynamic and electrodynamic model and use this model to explain the key parameters that control this phenomenon. Second, we will use the combined numerical model to match the observed evolution of SP prior to breakthrough and investigate possible causes of the precursor, in order to understand the broader applicability of SP as a predictor of SI.

2. SP Source Mechanisms

Numerous mechanisms can generate SPs, including electrokinetic, electrochemical, thermoelectric, piezoelectric, and redox processes (e.g., Jouniaux et al., 2009). At conditions close to thermodynamic equilibrium (Revil & Linde, 2011), the contributions of each source mechanism i can be related to total current flow j via the following generalized equation (Jackson, 2015; Jackson, Gulamali, et al., 2012; Saunders et al., 2008; Sill, 1983):

$$j = -\sigma_T \nabla V + \sum_i L_i \nabla U_i \tag{1}$$

where σ_T is the effective conductivity of the host material including matrix and pore space constituents (S/m), V is the electrical potential (V), U_i is the potential of the source mechanism (e.g., pressure and concentration), and L_i is the associated cross-coupling term. In the absence of SP source mechanisms, equation (1) is equivalent to Ohm's law. The cross-coupling term is often expressed in terms of a coupling coefficient C_i (Jackson, Gulamali, et al., 2012):

$$L_i = \sigma_T C_i. \tag{2}$$

In coastal aquifers, V_{EED} and V_{EK} are likely to be the most significant components of SP (MacAllister et al., 2016, 2018), because of respective variations in pressure induced by tidal fluctuations and in groundwater salinity, due to the presence of seawater at depth below comparatively fresh groundwater near the water table.

2.1. Electrokinetic Potential V_{EK}

An excess of charge typically occurs at mineral-water interfaces, which is balanced by an adjoining layer of opposing charge (counterions) within the fluid (Hunter, 1981). This arrangement is often referred to as the *electric double layer*. The fluid layer closest to the mineral surface (the Stern layer) is characterized by strongly sorbed counterions; the layer furthest from the mineral surface is known as the diffuse layer (or Gouy-Chapman layer) and is characterized by a lower density of charge, which is mobile and can be transported by flow (Revil et al., 1999).

In chalk saturated with groundwater or seawater, the surface charge is typically negative (Jackson, Butler, & Vinogradov, 2012; MacAllister, 2016) and groundwater flow from nonhydrostatic pressure gradients transports positively charged ions along the diffuse layer, leading to an electrokinetic current (Jackson, 2015) (Figure 1a). A conduction current arises to maintain overall electroneutrality, and V_{EK} represents the electrical potential required to sustain this current (Jackson, Gulamali, et al., 2012). In the absence of other current sources, equations (1) and (2) give (Jackson, 2015)

$$j_{\mathrm{EK}} = -\sigma_T \nabla V_{\mathrm{EK}} + \sigma_T C_{\mathrm{EK}} \nabla P_n \tag{3}$$

where P_n is nonhydrostatic pressure (Pa) and C_{EK} is the electrokinetic coupling coefficient (V/Pa), which in the absence of current flow is defined by

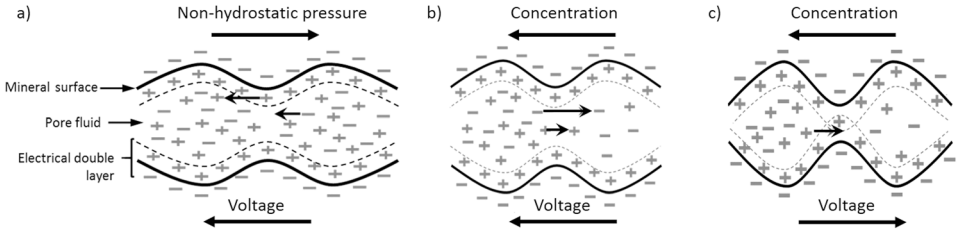

Figure 1. Pore-scale representation of (a) V_{EK}, (b) V_{ED}, and (c) V_{EE}(adapted from Jackson, Gulamali, et al., 2012).

$$\nabla V_{EK} = C_{EK} \nabla P_n. \tag{4}$$

The magnitude of C_{EK} decreases with concentration up to the concentration of seawater; in highly saline groundwater, counterions are closer to the mineral surface on average and a lower charge density is transported under a given (nonhydrostatic) pressure gradient (Jaafar et al., 2009; Vinogradov et al., 2010).

2.2. Exclusion-Diffusion Potential V_{EED}

In the absence of other current sources, equations (1) and (2) can be used to give V_{EED} (e.g., Jackson, 2015; Revil & Linde, 2006), which comprises a diffusion (or liquid junction) and an exclusion (or membrane) component:

$$j_{EED} = -\sigma_T \nabla V_{EED} + \sigma_T C_{EED} \nabla \ln C_f \tag{5}$$

where C_f is the molar fluid concentration (M) and C_{EED} is the electrochemical coupling coefficient (V). In the absence of current flow, this may be rewritten as (Leinov & Jackson, 2014; Revil, 1999)

$$\nabla V_{EED} = -\frac{k_B T}{e}(2T_+ - 1)\nabla \ln C_f \tag{6}$$

where T_+ is the macroscopic Hittorf number for cations (dimensionless), k_B is the Boltzmann constant (J/K), T is temperature (K), and e is the charge on an electron (C).

In the case of a salinity gradient in an uncharged porous medium, where the solute is dominated by sodium and chloride ions, charge separation is induced by the greater mobility of chloride, giving rise to an electrochemical diffusion potential (V_{ED}; e.g., Jackson, 2015; Revil, 1999; Figure 1b). In this scenario, the SP signal is effectively a diffusion potential and T_+ is equivalent to the microscopic Hittorf number for sodium, t_{Na}. Ignoring the weak concentration dependency of t_{Na}, and assuming a constant temperature, gives the following expression (Jackson, 2015; Leinov & Jackson, 2014):

$$\nabla V_{ED}\big|_{T_+ = t_{Na}} = -\frac{k_B T}{e}(2t_{Na} - 1)\nabla \ln C_f. \tag{7}$$

The following relation can be used to represent the slight changes in $t_{Na}$with ionic strength (Gulamali et al., 2011; Jackson, Gulamali, et al., 2012; Leinov & Jackson, 2014):

$$t_{Na} = \begin{cases} 0.39, & C_f < 0.09M \\ 0.366 - 2.12\times10^{-2} \log_{10} C_f, & C_f > 0.09M \end{cases}. \tag{8}$$

If the salinity gradient lies within a negatively charged porous medium and the electrical double layer is thick relative to the pore-throat radius, chloride ions are excluded from the pore space, leading to an exclusion potential V_{EE} (Figure 1c). In a perfect membrane, $T_+ = 1$, giving (Leinov & Jackson, 2014; Westermann-Clark & Christoforou, 1986):

$$\nabla V_{EE} = -\frac{k_B T}{e}\nabla \ln C_f. \tag{9}$$

The relative importance of the exclusion and diffusion components is defined by the dimensionless exclusion efficiency η (Leinov & Jackson, 2014; MacAllister, 2016; Westermann-Clark & Christoforou, 1986):

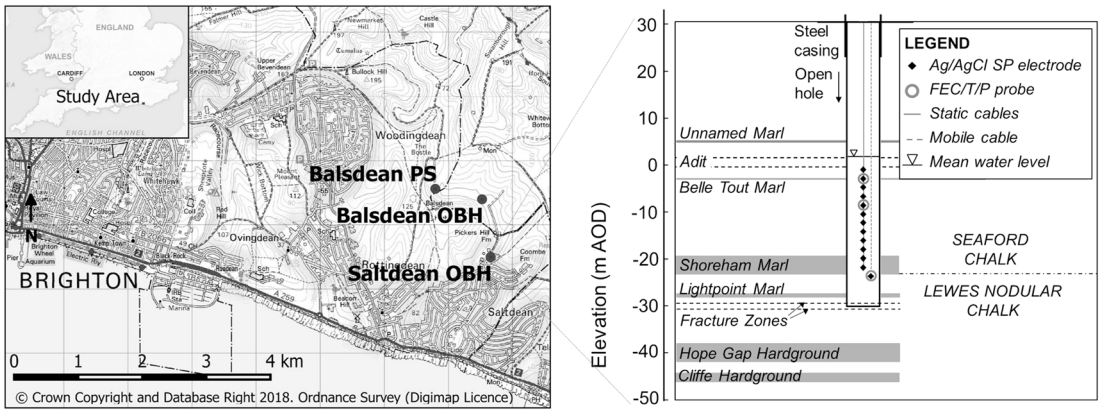

Figure 2. Map of study area and schematic of the Saltdean Observation Borehole (OBH). PS = Pumping Station; SP = self-potential.

$$\eta = \frac{\nabla V_{\mathrm{EED}} - \nabla V_{\mathrm{ED}}}{\nabla V_{\mathrm{EE}} - \nabla V_{\mathrm{ED}}}. \tag{10}$$

3. Site Characterization

A downhole array of SP electrodes was installed in May 2013 in the Saltdean OBH near Brighton on the south coast of England (Figure 2). The Saltdean OBH, which lies in a dry valley approximately 1.8 km from the coast, was formerly used as an abstraction borehole, but was abandoned in 1936 because of repeated saline intrusion (Jones & Robins, 1999). Borehole logs from the area suggest that an adit with a diameter of 1.4 m intersects the Saltdean OBH at −2 m above Ordnance Datum (AOD) and extends 32 m to the northwest, connecting the Saltdean OBH to two other groundwater boreholes nearby (BGS, 2018). The Saltdean OBH now acts as a monitoring borehole for the Balsdean Pumping Station (PS) further inland, which provides drinking water to the eastern part of Brighton.

3.1. Geology

The site lies within the South Downs, an area dominated by chalk strata that form part of the wider Chalk Group. The Saltdean OBH extends to 60 m below ground level, intersecting a series of chalk, marl, and hardground layers within the Seaford and Lewes Nodular Chalk Members of the White Chalk Subgroup (Figure 2). The strata dip gently toward the coast (Jones & Robins, 1999) at an angle of approximately 5°, based on the inferred depth of the Seaford-Lewes Nodular Chalk contact in the Saltdean OBH (AMEC, 2012) and at the PS (MWH, 2006).

3.2. Hydrogeology

3.2.1. Groundwater Flow

The majority of groundwater flow in the Chalk occurs within fractures (Allen et al., 1997; Bloomfield, 1996; MacDonald & Allen, 2001), where the hydraulic conductivity is typically several orders of magnitude higher than that of the surrounding matrix (Butler et al., 2012; Jones & Robins, 1999). Fractures may exist as faults, joints, or bedding planes, although the latter are considered to be the most pervasive and the most significant conduits for flow (Bloomfield, 1996).

Numerous, laterally extensive marl seams have been logged within the Chalk, which act as barriers to flow due to their relatively low hydraulic conductivity (Gallagher et al., 2012; Molyneux, 2012; Zaidman et al., 1999). Hardgrounds are often considered flow conduits, due to their brittle nature and enhanced fracturing (Schurch & Buckley, 2002; Soley et al., 2012), although they may also be barriers to flow when fracturing is minimal (Jones & Robins, 1999).

In general, the hydraulic conductivity of the Chalk decreases with depth and the most significant flow horizons typically occur within 50 m of the water table (Butler et al., 2009; Jones & Robins, 1999; Williams et al., 2006). Laterally, the Chalk is significantly more permeable in valleys than in interfluves (Jones & Robins, 1999;

MacDonald & Allen, 2001). Within the South Downs, the Seaford Chalk is considered to be the major water-bearing unit (Jones & Robins, 1999).

According to Jones and Robins (1999), logging of the Saltdean OBH has indicated a hydraulically significant fracture at its base, which constitutes the main conduit for SI. This was later supported by MacAllister et al. (2018), who showed through a series of σ_f profiles that saline water enters near the base of the borehole and exits via the adit near the top of the water column.

Recharge estimates vary across the South Downs, although in the Brighton Block, where the Saltdean OBH is located, Jones and Robins (1999) report a mean value of around 480 mm/yr. The majority of recharge occurs during the winter months, with limited (Ireson et al., 2009; Wellings, 1984) or no recharge (Limbrick, 2002) between May and September. Despite the minimal flow occurring in the unsaturated zone during this period, the narrow pore-throat diameters in the Chalk matrix imply that it remains almost entirely saturated within 30 m of the water table (Price, 1987), although dewatering of the fractures occurs, typically accounting for less than 1% of the total rock volume (Butler et al., 2012; Mathias, 2005; Price, 1987).

3.2.2. Aquifer Properties

The median storage coefficient in the South Downs Chalk, as reported by MacDonald and Allen (2001) is 0.0022 and the mean porosity of the White Chalk Subgroup in the south of England is 39% (Bloomfield et al., 1995).

Based on observed drawdown at the Balsdean PS, MWH (2006) inferred a hydraulic conductivity K of 900 m/day for the surrounding aquifer, significantly higher than the median value of 9 m/day for the South Downs as a whole (based on the median transmissivity of 880 m^2/day reported by MacDonald and Allen (2001) and an assumed aquifer thickness of 50 m). We estimate here a hydraulic conductivity of 250 m/day, based on a mean lag $\tau$of 0.152 days between tidal peaks observed at the coast (in Newhaven, 7 km to the southeast; British Oceanographic Data Centre, 2015) and using (Jacob, 1950):

$$K = \frac{t_0 S x^2}{4\pi b \tau^2} \tag{11}$$

where t_0 is the semidiurnal period of tidal fluctuation (0.518 days; MacAllister et al., 2016), S is storativity (0.0022), x is distance from the coast (1,800 m), and b is aquifer thickness (50 m).

3.3. Electrical Parameters

Rearranging equations (5)–(7), (9), and (10), assuming no current flow, gives the following expression for C_{EED} in a fully saturated medium:

$$C_{EED} = -\frac{k_B T}{e}[(\eta + 1)(2t_{Na} - 1) - \eta] \tag{12}$$

MacAllister (2016) measured η in Seaford (0.01–0.12) and Lewes Nodular Chalk (0.02–0.06) cores saturated with local groundwater and seawater, although no direct measurements of η are available for marls and hardgrounds, which lie beneath the Saltdean study area. These values can be inferred based on observed changes in σ_f and SP with depth in the Victoria Gardens borehole, 7 km west of Saltdean (see supporting information Figure S1).

Values of σ_f in mS/cm are converted to total dissolved solids in mg/L (TDS), using the following relation (Walton, 1989):

$$TDS = 700\sigma_f. \tag{13}$$

Measurements of TDS for seawater (34,113 mg/L) and groundwater (376 mg/L) are compared to calculated values of C_f (0.673 for seawater; 0.00851 for groundwater) reported by MacAllister (2016) giving

$$Cf \approx 2.12 \times 10^{-5} TDS. \tag{14}$$

Applying the variations in $C_f$and SP to equations (7) and (9) and assuming the variations in SP within the borehole are representative of ∇V_{EED} within the adjacent formation gives estimates of η for the Shoreham Marl (0.15), the Hope Gap Hardground (0.21), and the Lewes Marl (0.28) using equation (10). These findings are consistent with previous studies (Leinov & Jackson, 2014; MacAllister, 2016; Westermann-Clark &

Christoforou, 1986), which suggest that lithologies with relatively narrow pore-throat diameters, such as shale (Nelson, 2009), marls, and hardgrounds (Fay-Gomord et al., 2016) typically have higher values of η. Indeed, the value of η for shale (0.24) reported by MacAllister (2016) is similar to the values derived for marls and hardgrounds.

Vinogradov et al. (2010) showed that $|\ln(C_{EK})|$varies linearly with $\ln(C_f)$ in fully saturated core samples below seawater salinity. Using measurements of C_{EK} for local groundwater (-5.12×10^{-6} V/Pa) and seawater (-1.76×10^{-7} V/Pa) reported by MacAllister (2016), we obtain

$$C_{EK} = -1.286 \times 10^{-9} C_f^{-0.769}. \tag{15}$$

The electrical conductivity of the Chalk aquifer σ_T can be estimated using Archie's law (Telford et al., 1990):

$$\sigma_T = \phi^m \sigma_f S_w^2 \tag{16}$$

where m is the cementation exponent, ϕ is porosity, and$S_w$is saturation. MacAllister (2016) derived values for m of 2.1–2.6 from core samples of Seaford and Lewes Nodular Chalk.

The presence of clay minerals increases electrical conductivity; this can be accounted for using the empirical Waxman-Smits equation (Darling, 2005), originally developed for shaly sands:

$$\sigma_T = \phi^m \sigma_f S_w^2 \left(1 + B\left(\frac{\rho_m CEC}{100 \phi \sigma_f S_w}\right)\right) \tag{17}$$

where ρ_m is the mineral grain density (Fay-Gomord et al., 2016, report values of 2.7 g/cm for marl), *CEC*is the cation exchange capacity (averaging 9.5 mEq/100 g for a typical marl; Cornell & Aksoyoglu, 1991) and

$$B = \left(-1.28 + 0.255 T_C - 0.0004059 {T_C}^2\right) / \left(1 + \frac{(0.04 T_C - 0.27)}{\sigma_f^{-1.23}}\right) \tag{18}$$

where T_C is temperature in degrees Celsius, which remains close to 11°C in the Saltdean OBH throughout the monitoring period.

4. Monitoring Apparatus and Data Processing

An array of 13 nonpolarizing Silvion Ag/AgCl WE300 electrodes was installed in the Saltdean OBH from May 2013 to February 2015 (Figure 2). The shallowest of these was installed at −2.8 mAOD and used as a reference electrode throughout, with the remaining electrodes spaced at 2-m intervals below it. The deepest electrode was installed separately from the others at −26.8 mAOD, along with an AquaTroll 200 probe which recorded temperature T, σ_f, and pressure P; several vertical profiles of SP and σ_f were collected over the monitoring period using this *traveling electrode*. Two further AquaTroll probes were installed at −4.8 mAOD and −10.8 mAOD respectively to record vertical changes in T, σ_f, and P. The monitoring apparatus was connected to a Campbell Scientific CR3000 data logger, which collected data at 5-min intervals. Further details on the equipment used and data collection methods are given by MacAllister et al. (2016).

The raw SP data include semidiurnal oscillations consistent with the M2 component of oceanic tides, which dominate the signal (MacAllister et al., 2016). A first-order Savitsky-Golay (SG) moving average filter, with a sampling window of 2.2 days, was applied to the data to assist in identifying longer-term trends in the SP data set. The SG filter has previously been used for SP analysis (e.g., MacAllister, 2016; Maineult et al., 2008) and has the advantages of maintaining the shape and amplitude of lower frequency oscillations, without introducing phase delay (Savitsky & Golay, 1964).

In addition to the long-term monitoring conducted at the Saltdean OBH, vertical SP profiles were collected from the Balsdean OBH around 1 km further inland (Figure 2a) and from borehole PL10B, located at Trumpletts Farm in Berkshire, more than 60 km from the coast (MacAllister et al., 2018). All three boreholes intersect the Seaford and Lewes Nodular Chalk, allowing a comparison of SP profiles in a similar geological setting, at varying distances from the coast.

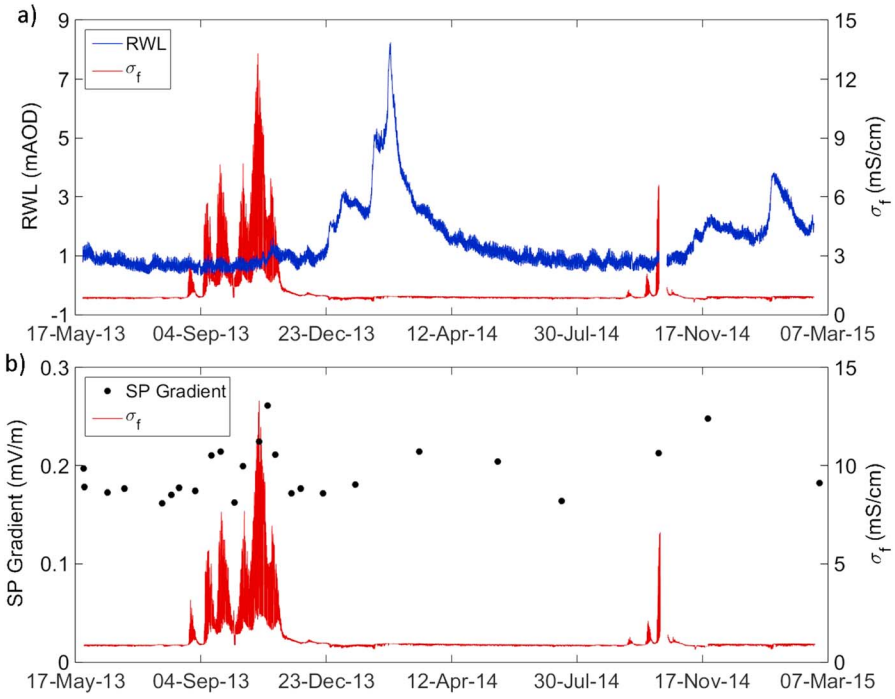

Figure 3. Data from the Saltdean Observation Borehole, comprising (a) σ_f and reduced water levels (RWLs; converted from pressure recorded at −26.8 m above Ordnance Datum, AOD); and (b) σ_f and self-potential (SP) gradients across the water column, calculated from vertical profiles taken with the traveling electrode and referenced to the shallowest borehole electrode.

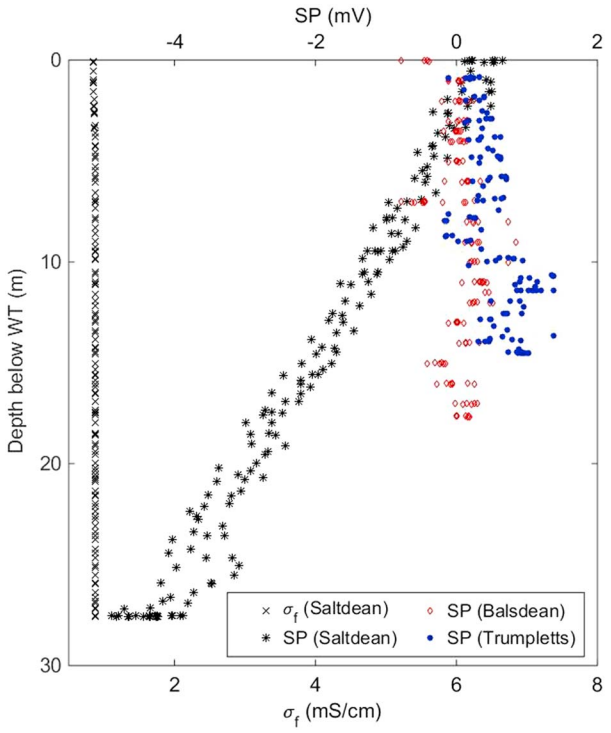

Figure 4. Self-potential (SP) profiles from the Saltdean Observation Borehole (OBH), Balsdean OBH, and Trumpletts borehole, along with σ_f in the Saltdean OBH.

5. Summary of Field Data

The data recorded by the deepest $T/\sigma_f/P$ probe show that saline water entered the Saltdean OBH in late summer/early autumn of both 2013 and 2014 (Figure 3a). These events occurred following prolonged periods of low water levels in the borehole; intrusion ceased at the commencement of the winter recharge period, as shown by the higher water levels from November onward.

The potential gradient across the water column (based on vertical profiles taken by the traveling electrode) remained close to 0.2 mV/m throughout the monitoring period (Figure 3b). The respective SP gradients in the Balsdean OBH and Trumpletts borehole, which both lie further inland, are minimal by comparison (Figure 4). The σ_f in the Saltdean OBH was approximately 0.87 mS/cm throughout the water column (~610 mg/L, from equation (13)).

SP across the water column decreases by 0.2–0.3 mV several days prior to intrusion (Figure 5); this *precursor* is most apparent in the 2013 data. These precursors also appear in the 2014 data, although the occurrence of what appear to be two minor intrusion events prior to more obvious saline breakthrough on 12 September leads to a more complex pattern of both salinity and SP.

As well as the intrusion of saline water when water levels are low, a smaller increase in salinity occurs in conjunction with major recharge events, indicating the presence of elevated salinity above the water table (Figure 6). This influx of more saline water is preceded by a sharp reduction in σ_f of short duration. This may reflect distinct contributions from (i) rapid

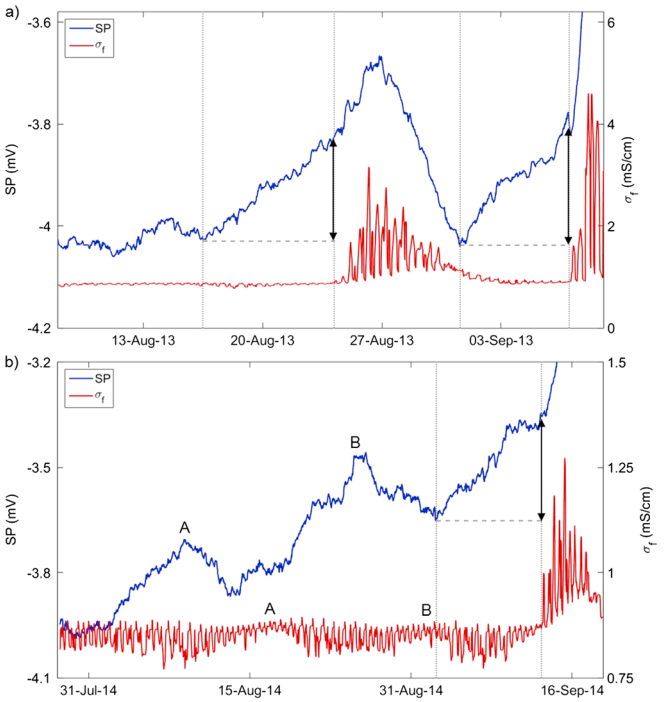

Figure 5. Transient self-potential (SP) and σ_f in the Saltdean Observation Borehole around the time of saline intrusion in (a) 2013 and (b) 2014. All data were collected from −26.8 m above Ordnance Datum. Characteristic increases in SP prior to intrusion are highlighted by dotted gray lines and arrows. Similar SP responses, marked *A* and *B* in (b), can be seen prior to minor intrusion events.

bypass flow in the fractures, delivering relatively fresh recharge to the borehole, and (ii) piston flow, yielding more mineralized recharge, as a result of prolonged interactions between percolating rainwater and the rock matrix (see Jones & Robins, 1999).

6. Model Description

An electrodynamic model was produced to investigate the static SP gradient (Figure 5) and variations in SP prior to intrusion (Figure 6) in the Saltdean OBH. The electrodynamic model relies on distributions of pressure and salinity (see equations (3)–(6)), which are provided by an accompanying hydrodynamic model of the coastal Chalk aquifer.

6.1. Hydrodynamic Model

Hydrodynamic simulations were conducted using SUTRA3D (Voss & Provost, 2002), one of the most widely used models for simulating density-driven flow and transport (Werner et al., 2013). Three model domains were used (Figure 7) to simulate pressure and salinity variations at the coast, while giving a detailed 3-D representation of the geology around the borehole, consistent with the stratigraphy and fracture zones shown in Figure 2.

The model was run initially with long-term average conditions until a steady state distribution of salinity was achieved. This steady state model provided the initial conditions for a transient model, which includes tidal oscillations in pressure at the coast and invokes saline intrusion by turning off recharge after 7 days of the simulation.

Parameterization of the model is consistent with the site characterization in sections 3.1 and 3.2. A detailed description of the parameters applied to the hydrodynamic model, along with time stepping and solver parameters, is given in supporting information Text S2.

Pressure and salinity distributions produced by the hydrodynamic model were used to calculate SP within the electrodynamic model described in the following section.

6.2. Electrodynamic Model

6.2.1. Initial Data Processing

The electrodynamic model was written in MATLAB, using the controlled volume finite difference method, and is based on the approach of Gulamali et al. (2011), Ijioma and Jackson (2014), and Jackson, Gulamali,

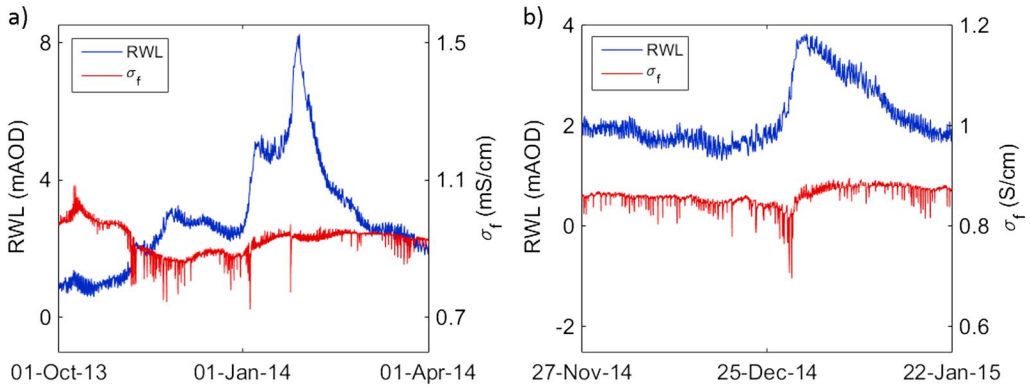

Figure 6. Fluctuations in σ_f following major recharge events in (a) late 2013/early 2014 and (b) late 2014/early 2015. A short-lived reduction in σ_f occurs as water levels begin to rise, followed by a more sustained increase in σ_f. RWL = reduced water level; AOD = above Ordnance Datum.

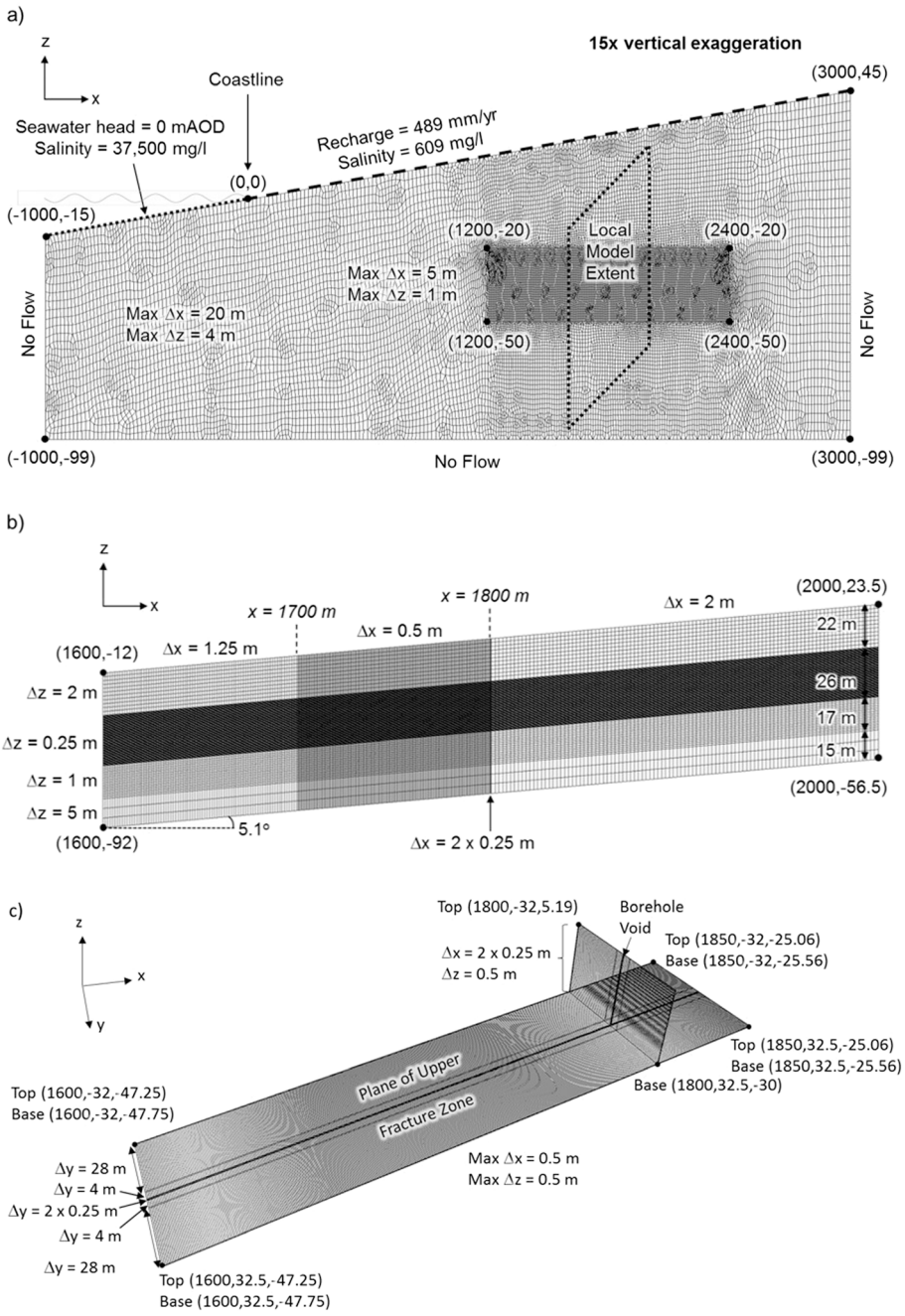

Figure 7. Finite element meshes for (a) the 2-D regional model, including steady state boundary conditions, (b) the 2-D local model, and (c) the 3-D model of the borehole and plane of the upper fracture zone.

et al. (2012) for modeling SP in hydrocarbon reservoirs. It solves equations (3) and (5) for V_{EK} and V_{EED}, assuming no external current sources or sinks, such that

$$j|_\Gamma = \nabla P_n|_\Gamma = \nabla \ln C_f|_\Gamma = 0 \tag{19}$$

at the model boundaries. Modeled SP is obtained by adding the contributions of V_{EK} and V_{EED}.

The model begins by mapping pressures and concentrations from the 2-D local model onto the logically rectangular mesh shown in Figure 8 and assuming no variation in the *y* direction. It then incorporates data for the region covered by the 3-D hydrodynamic model. The top 40 elements in Figure 8 lie above the extent of the 2-D local and 3-D hydrodynamic models; parameterization of this region is described in section 6.2.2.

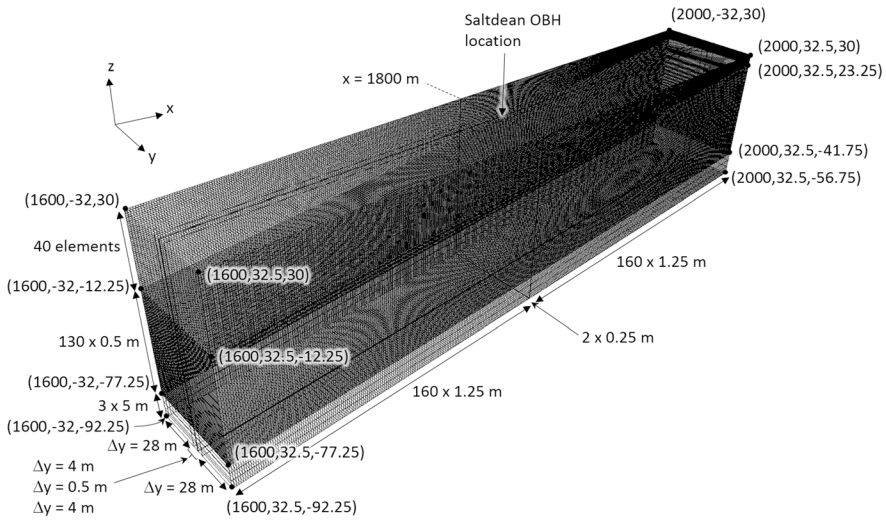

Figure 8. Finite element mesh for the electrodynamic model. OBH = Observation Borehole.

Hydrostatic pressure P_h was inferred by taking the nodal pressure values at the base of the fortieth element P_{40}, calculating the arithmetic mean of fluid density ρ_f between each element below them and invoking

$$\Delta P_h = \rho_f g \Delta z \tag{20}$$

where g is the acceleration due to gravity (9.81 m/s^2), $\Delta z$is the change in elevation between elements, andρ_f is linearly interpolated from the density of fresh water (1,000 kg/m^3 for 0 mg/L) and sea water (1,025 kg/m^3 for 35,000 mg/L). The nonhydrostatic pressure component P_n was obtained by subtracting P_h from the total pressure at the center of each element.

Spuriously low or high salinities produced by numerical oscillations in the SUTRA model were removed by limiting minimum and maximum concentrations to 609 mg/L and 35,000 mg/L, respectively. To mimic the rate of breakthrough shown in Figure 6 and avoid minor fluctuations in borehole salinity prior to this, all salinity values below 700 mg/L were set equal to 609 mg/L.

As the front within the 2-D local SUTRA model was more dispersed than that within the 3-D model (see supporting information Text S2), the advancing salinity within the upper fracture zone (shown in Figure 2) led to spurious elevated concentrations within the overlying strata at later time steps. To avoid this, the salinity distribution for the start of the transient model was maintained throughout for elements, which lie less than 2.5 m above the upper fracture zone.

Modeled porosity was 0.39 throughout the model domain, except in the borehole and adit, where a value of 1 was applied.

6.2.2. Unsaturated Zone

Where the water table lies above the top of the SUTRA local model, its elevation was inferred from equation (20) and values of P_{40}, assuming hydrostatic conditions and a constant fluid density of 1,000.435 kg/m^3 (consistent with a fluid concentration of 609 mg/L). Saturation was reduced from 1 to 0.995 over the two elements immediately above the water table to reflect dewatering of fractures and concentration was increased linearly to 2,200 mg/L over a further two elements above this, reflecting the presence of elevated salinity in the unsaturated zone (Figure 6). Constant values of saturation (0.995) and concentration (2,200 mg/L) were maintained above this.

6.2.3. Electrical Parameters

TDS concentrations were converted to σ_f and C_f using equations (13) and (14).

The bulk electrical conductivity of the aquifer was simulated using equation (16), with a value of 2.5 for the cementation exponent m below the unnamed marl and a value of 1.5 above this, reflecting an increased degree of fracturing at shallow depths and, hence, greater connection between pores (Glover, 2009; Roubinet et al., 2018). For marl seams, equation (17) was applied, reflecting the contribution of surface conductance in clay minerals.

Table 1
Modeled Exclusion Efficiencies η

Feature	η
Seaford Chalk	0.09
Lewes Nodular Chalk (above lower fracture zone)	0.03
Lewes Nodular Chalk (≤3.5 m below lower fracture zone)	0.01
Lewes Nodular Chalk (>3.5 m below lower fracture one)	0.05
Shallow Marls (above base of borehole)	0.15
Deep Marls and Hardgrounds (below base of borehole)	0.24
Borehole void, adit, and fracture zones	0.00

The values of the coupling coefficients C_{EED} and C_{EK} were obtained from equations (12) and (15); the values of η applied to equation (15) are shown in Table 1.

7. Model Results and Discussion

Steady state SP within the borehole is compared to the observed profile in Figure 9a. The modeled profile is dominated by V_{EED} and the contribution of V_{EK} is negligible by comparison, consistent with the previous study of MacAllister et al. (2018).

The sensitivity of the SP gradient to multiple input parameters is shown in Figure 9b. Increasing recharge by 25% produces a deeper saline front and reduces the SP gradient substantially. Removing variations in η has a more pronounced effect on SP and in the case of a constant value of η (0.04) throughout the model domain, the SP gradient ahead of the front disappears.

The removal of elevated salinity (and hence electrical conductivity) in the unsaturated zone also lowers the modeled gradient. The elevated electrical conductivity of clay minerals in the marl bands does not greatly affect the magnitude of the SP gradient, although it does appear to be responsible for the deviation in observed SP adjacent to the Shoreham Marl, just below −20 mAOD.

The results suggest that the observed SP gradient relies both on a nearby saline front and local variations in η. Given the extremely low permeability of the chalk matrix, the presence of a nearby saline front may reflect historic SI over a period of many years. While these historic events would suggest a high risk of future intrusion, it is difficult to infer the timing of future events from a single SP profile. To this end, the evolution of the SP gradient could provide a better indication of imminent SI.

Field observations of the precursor are compared to the results of the best fit model and sensitivity analyses in Figure 10. This includes (on the left-hand side) raw model outputs and field data with a short-period SG filter applied to remove high-frequency noise; and (on the right-hand side) field and model data with a 2.2-day SG filter applied to remove the effects of tidal oscillations. The results from the best fit model

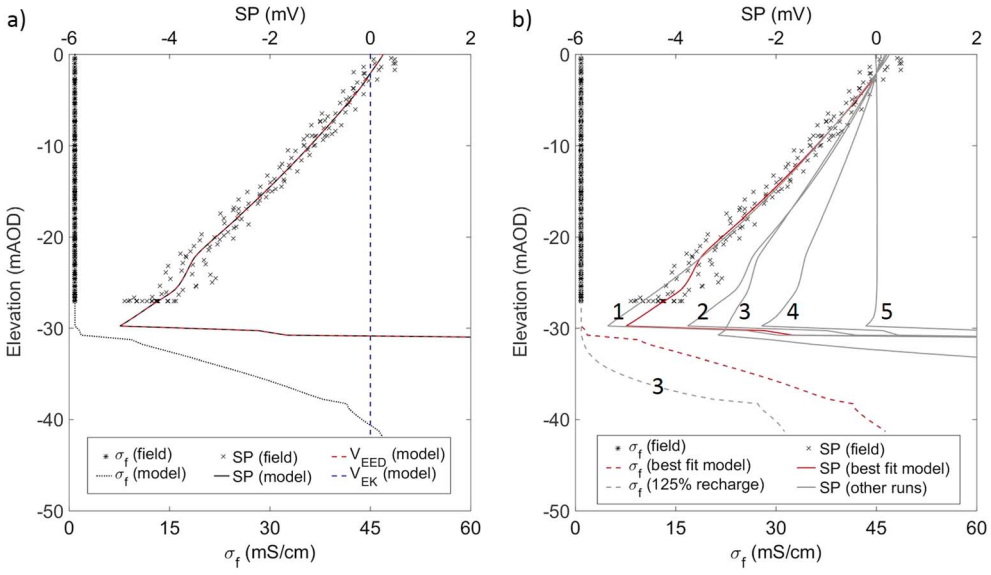

Figure 9. Comparison of observed and simulated self-potential (SP) and σ_f profiles. (a) Best fit model results, showing the contribution of V_{EED} and V_{EK} components. (b) Sensitivity analysis showing the effects of (1) representing formation conductivity in the marl horizons using Archie's law (cf. Waxman-Smitts), (2) applying a fluid concentration of 609 mg/L throughout the unsaturated zone, (3) increasing steady state recharge by 25%, (4) applying η = 0.04 for all chalk layers (excluding marls and hardgrounds), and (5) applying η = 0.04 for all chalk, marl, and hardground layers. AOD = above Ordnance Datum.

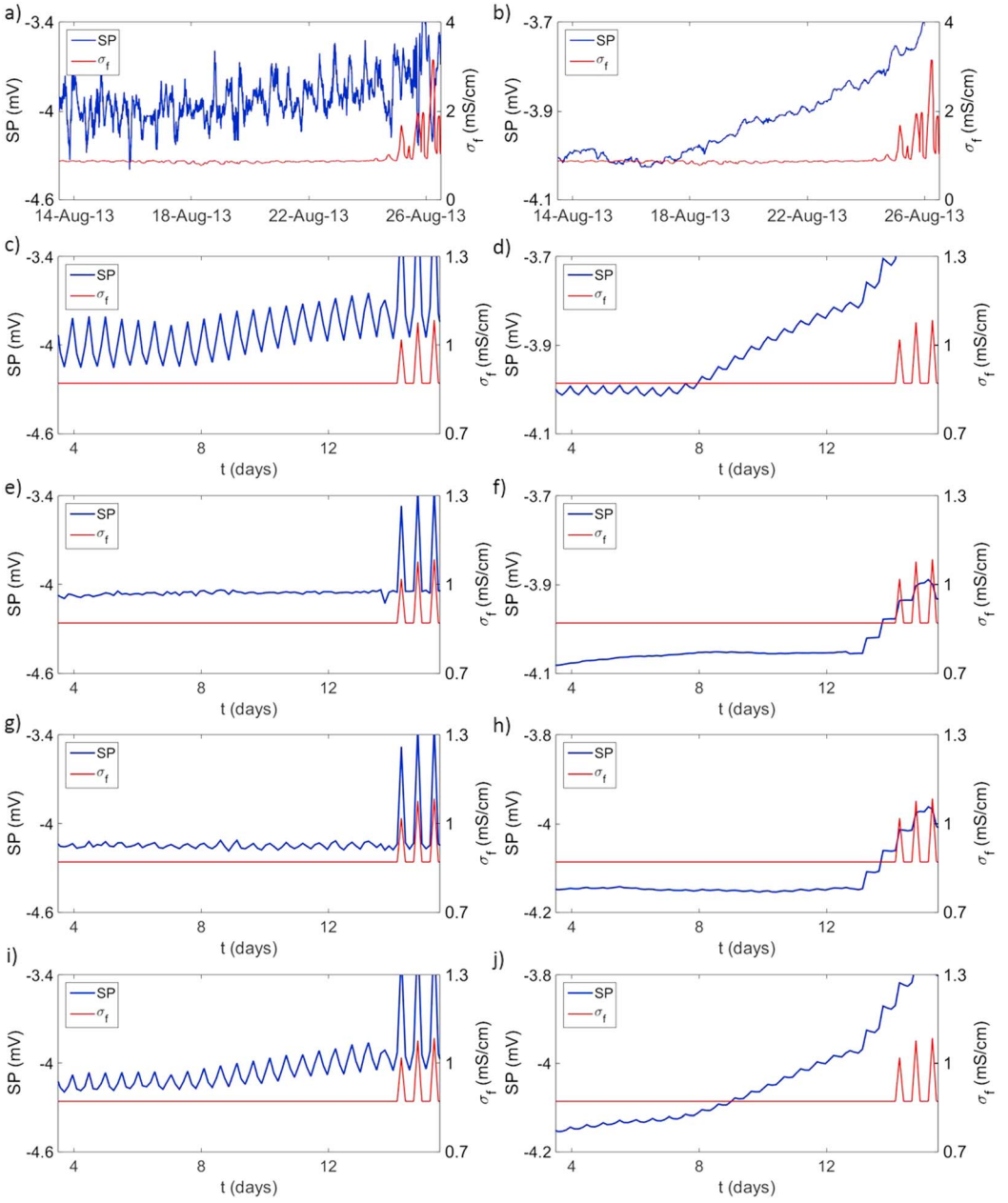

Figure 10. Observed and simulated self-potential (SP) precursors. (a) Field SP and σ_f data (Savitsky-Golay, SG, filter with a 105-min sampling window applied to reduce high-frequency noise). (b) Field SP and σ_f data (SG filtered, 2.2-day sampling window). (c) Best fit model SP and σ_f (unfiltered). (d) Best fit model results (SG filtered, 2.2-day sampling window). (e) Model sensitivity analysis: Fixed salinity distribution in the lower fracture zone throughout (unfiltered). (f) As in (e), with a 2.2-day SG filter. (g) Model sensitivity analysis: η = 0.01 above and below lower fracture zone (unfiltered). (h) As in (g), with a 2.2-day SG filter. (i) Model sensitivity analysis: η = 0.01 above and below upper fracture zone and fixed salinity in lower fracture zone. (j) As in (i), with a 2.2-day SG filter.

(Figures 10c and 10d) closely match observations for summer 2013 (Figures 10a and 10b). The smaller magnitude of $\sigma_f$peaks following breakthrough in the model highlights the propensity for numerical models to produce highly dispersed fronts (Konikow, 2011).

Sensitivity analysis in the model provides an important insight into the likely mechanisms that drive the precursor. The first analysis investigates the contribution of the inferred lower fracture zone in Figure 2 to the evolution of SP. This is achieved by treating the lower fracture zone as a region of low permeability,

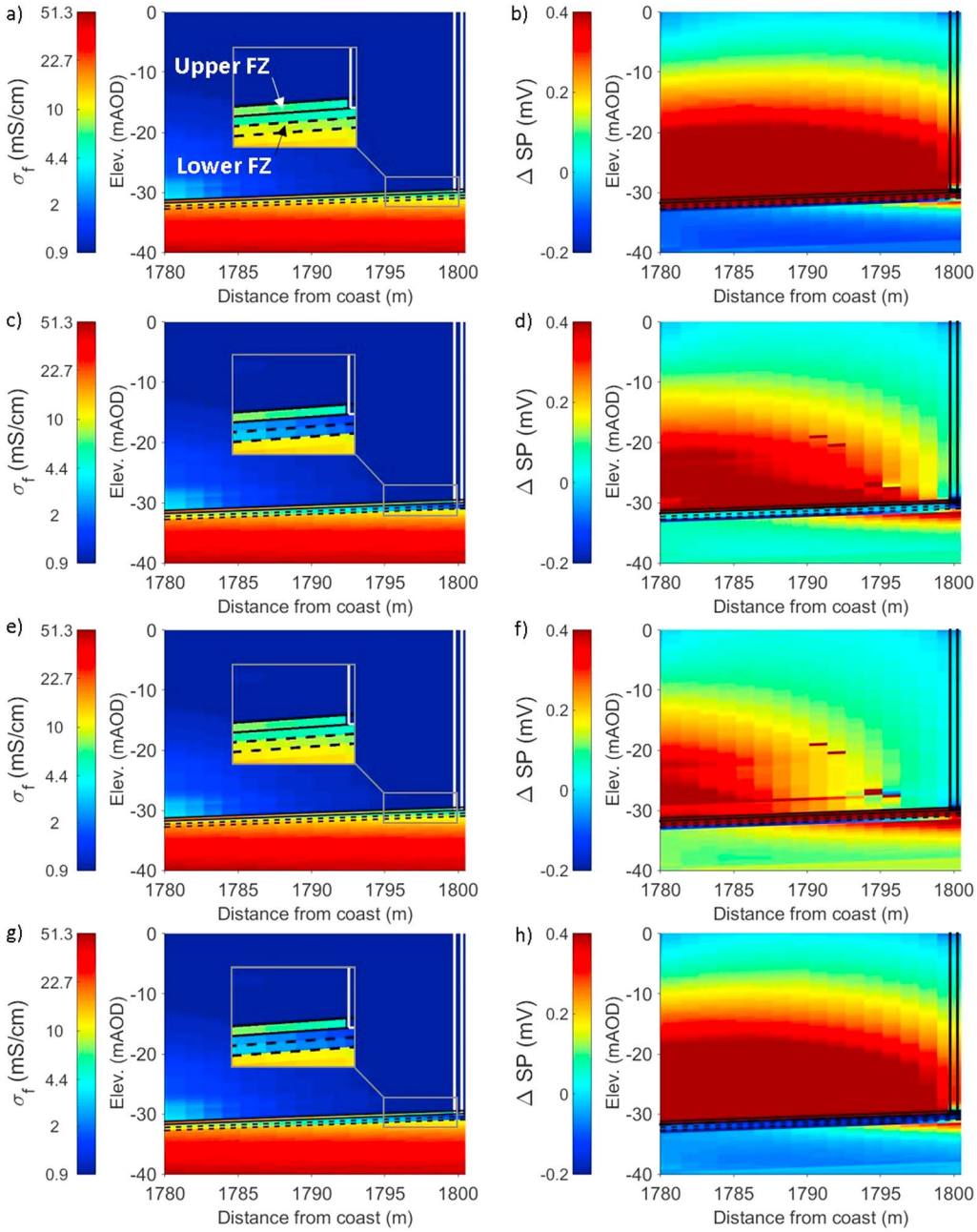

Figure 11. Modeled distributions of σ_f (a, c, e, and g) and changes in self-potential (SP) relative to initial conditions (b, d, f, and h) immediately prior to saline breakthrough (t = 14.2 days). (a, b) Best-fit model, with a dynamic lower fracture zone intersecting strata of differing η; (c, d) as in (a) and (b), with a static saline front in the lower fracture zone; (e, f) as in (a) and (b) with η = 0.01 across the lower fracture zone; and (g, h) as in (a) and (b), with static lower fracture zone and differing η across the upper fracture zone. The outlines of the borehole (solid lines), the upper fracture zone (solid lines), and the lower fracture zone (dashed lines) are also shown. The limits of the ΔSP color scale have been curtailed to emphasize changes in SP within the borehole. AOD = above Ordnance Datum.

unfractured chalk, and modeling the initial salinity distribution in this layer throughout the transient model (while allowing the saline front to evolve freely throughout the rest of the model domain). As shown in Figures 10e and 10f, this completely removes any precursor to intrusion.

However, movement of salinity beneath the borehole is not sufficient by itself to produce a precursor. Applying η = 0.01 on both sides of the lower fracture zone also removes the modeled precursor

(Figures 10g and 10h). The precursor therefore reflects the movement of salinity through a heterogeneous geoelectric environment.

A precursor is also obtained by applying the variation in η values (from 0.01 below to 0.03 above) across the upper fracture zone (Figures 10i and 10j). In this scenario, a static front was maintained in the lower fracture zone, so movement of saline water within the upper fracture zone was the source of the modeled precursor. However, although the smoothed precursor is similar to that observed in the borehole, tidal oscillations are notably smaller in magnitude than those observed in the field and in the best fit model.

Figure 11 shows the saline front near the borehole and changes in SP (relative to the steady state model) immediately prior to SI. In each case, the saline front within the upper fracture zone lies <1 m laterally from the base of the borehole, on its seaward side. Figures 11a and 11b, which represent the best fit model, show how the SP gradient in the borehole is affected ahead of the saline front within the upper fracture zone. When a static front is applied to the lower fracture zone only, changes to the vertical SP gradient occur directly above the saline front within the upper fracture zone, with minimal changes ahead of it (Figures 11c and 11d), thereby giving no clear precursor (as shown in Figure 10e).

When the best fit model is modified by applying $\eta = 0.01$ on either side of the lower fracture zone, changes in the vertical SP gradient lag behind the advancing saline front in the upper fracture zone (Figures 11e and 11f). Finally, by applying a change in η across the upper instead of lower fracture zone and implementing a static front in the lower fracture zone (Figures 11g and 11h), the changes in SP are similar to those seen in the field and in the best fit model.

The results from the transient model suggest that the precursor is driven by small spatial changes in η across one or more conduits for saline intrusion. As shown in Figures 11e and 11f, the SP source conduit may intersect the borehole, or it may lie immediately beneath it (Figures 11a and 11b).

In the latter scenario, the precursor does not directly reflect the movement of seawater that will enter the borehole. However, geophysical logging and hydraulic testing (e.g., Butler et al., 2009; Gallagher et al., 2012; Jones & Robins, 1999) suggests that there are typically numerous hydraulically significant fractures within the upper 100 m of the Chalk. SI in the Chalk (and other fractured coastal aquifers) may therefore be characterized by saline water filling progressively shallower fracture zones. Thus, the arrival of higher salinity groundwater immediately beneath the borehole would be a strong but indirect indicator of imminent breakthrough into the borehole itself.

At present, a precursor of this nature has been observed only at a single site, making it difficult to assess the broader applicability of SP monitoring to predict SI. Furthermore, there are very few data on η, so the prevalence and magnitude of small-scale variations in η around a typical borehole is unknown. Other parameters, such as clay content and permeability, are highly variable in the Chalk and most other common aquifer lithologies over distances of only a few millimeters. Consequently, there are grounds for optimism that variations in η are also common and so SP precursors to SI may indeed be widespread. Further data collection is required to identify the presence (or otherwise) of precursors in other boreholes.

Based on the sensitivity of the model and our experience of SP monitoring, it is important that nonpolarizing Ag/AgCl or Pb/PbCl electrodes (see Perrier et al., 1997) are used to collect long-term SP data sets, to reduce problems with electrode drift that may complicate subsequent analysis. MacAllister (2016) and MacAllister et al. (2016) provide additional detail on the requirements for monitoring SP in a coastal aquifer.

8. Conclusions

Data collected from a groundwater observation borehole in a coastal aquifer near the south coast of England show a strong and consistent SP gradient ahead of a saline front. There is a characteristic reduction in this gradient several days prior to SI in the borehole. If present in other boreholes, this precursor could act as a warning system for groundwater users and may allow sufficient time to mitigate the risk of SI occurring.

The combined hydrodynamic and electrodynamic model developed in this study closely matches the phenomena observed in the field, using plausible values for the numerous input parameters. Through sensitivity analysis, it is clear that the SP gradient requires a nearby saline front and local variations in the exclusion efficiency, a parameter which will require further measurements to understand its distribution

and variability in different aquifer types. The precursor signal modeled here also relies on local variations in exclusion efficiency on either side of a fracture zone transmitting seawater inland. The fracture zone may either intersect the borehole, or be located immediately below it, although only the latter scenario replicates the observed magnitude of tidal SP variations. Further analysis should focus on tidal SP variations and how they evolve prior to SI.

The results are a promising first step in demonstrating the possible use of SP as a predictor of SI, although data from additional sites are required to demonstrate its widespread applicability.

Acknowledgments
This work was supported by the Natural Environment Research Council in the UK, as part of the Science and Solutions for a Changing Planet Doctor Training Partnership, run by the Grantham Institute for Climate Change at Imperial College London. We thank Southern Water for access to the boreholes at Saltdean and Balsdean. We thank Southern Water and Atkins Global for funding the installation of the equipment. We also thank Amadi Ijioma for providing a prototype of the electrodynamic modeling code in MATLAB, which has since been adapted for use in a coastal chalk aquifer. Three anonymous reviewers are thanked for their comments, which greatly helped to improve the manuscript. The data used in this paper are in the tables, figures, and cited information. The authors have no conflicts of interest to declare.

References

Allen, D. J., Brewerton, L. J., Coleby, L. M., Gibbs, B. R., Lewis, M. A., MacDonald, A. M., et al. (1997). The physical properties of major aquifers in England and Wales, British Geological Survey. WD/97/034**:** 333.

AMEC (2012). Lewes Winterbourne NEP investigation: Brighton and Worthing Groundwater modelling study conceptual model report, Environment & Infrastructure Report No. 29388rr297i1.

Barlow, P. M., & Reichard, E. G. (2010). Saltwater intrusion in coastal regions of North America. *Hydrogeology Journal*, *18*(1), 247–260. https://doi.org/10.1007/s10040-009-0514-3

BGS (2017). Wireline log of TQ30SW_3 Victoria gardens borehole. © NERC. All rights reserved.

BGS (2018). Geology of Britain viewer: Borehole scan of TQ30SE13. Retrieved Accessed 10 January 2018., Available at: http://mapapps.bgs.ac.uk/geologyofbritain/home.html

Bloomfield, J. (1996). Characterisation of hydrogeologically significant fracture distributions in the Chalk: An example from the Upper Chalk of southern England. *Journal of Hydrology*, *184*(3–4), 355–379. https://doi.org/10.1016/0022-1694(95)02954-0

Bloomfield, J. P., Brewerton, L. J., & Allen, D. J. (1995). Regional trends in matrix porosity and dry density of the Chalk of England. *Quarterly Journal of Engineering Geology and Hydrogeology*, *28*(Supplement_2), S131–S142. https://doi.org/10.1144/GSL.QJEGH.1995.028.S2.04

Bocanegra, E., Da Silva, G. C., Custodio, E., Manzano, M., & Montenegro, S. (2010). State of knowledge of coastal aquifer management in South America. *Hydrogeology Journal*, *18*(1), 261–267. https://doi.org/10.1007/s10040-009-0520-5

British Oceanographic Data Centre (2015). UK tide gauge network. Accessed 08/06/15. https://www.bodc.ac.uk/data/hosted_data_systems/sea_level/uk_tide_gauge_network/

Butler, A. P., Hughes, A. G., Jackson, C. R., Ireson, A. M., Parker, S. J., Wheater, H. S., & Peach, D. W. (2012). Advances in modelling groundwater behaviour in Chalk catchments. *Geological Society, London, Special Publications*, *364*(1), 113–127. https://doi.org/10.1144/SP364.9

Butler, A. P., Mathias, S. A., Gallagher, A. J., Peach, D. W., & Williams, A. T. (2009). Analysis of flow processes in fractured chalk under pumped and ambient conditions (UK). *Hydrogeology Journal*, *17*(8), 1849–1858. https://doi.org/10.1007/s10040-009-0477-4

Comte, J.-C., & Banton, O. (2007). Cross-validation of geo-electrical and hydrogeological models to evaluate seawater intrusion in coastal aquifers. *Geophysical Research Letters*, *34*, L10402. https://doi.org/10.1029/2007GL029981

Cornell, R. M., & Aksoyoglu, E. S. (1991). Simultaneous determination of the cation-exchange capacity and the exchangeable cations on marl. *Clay Minerals*, *26*(04), 567–570. https://doi.org/10.1180/claymin.1991.026.4.10

Custodio, E. (2010). Coastal aquifers of Europe: An overview. *Hydrogeology Journal*, *18*(1), 269–280. https://doi.org/10.1007/s10040-009-0496-1

Darling, T. (2005). *Well logging and formation evaluation*. Amsterdam, The Netherlands: Elsevier.

Fay-Gomord, O., Soete, J., Katika, K., Galaup, S., Caline, B., Descamps, F., et al. (2016). New insight into the microtexture of chalks from NMR analysis. *Marine and Petroleum Geology*, *75*, 252–271. https://doi.org/10.1016/j.marpetgeo.2016.04.019

Fitterman, D. V. (2014). Mapping saltwater intrusion in the Biscayne aquifer, Miami-Dade County, Florida using transient electromagnetic sounding. *Journal of Environmental and Engineering Geophysics*, *19*(1), 33–43. https://doi.org/10.2113/JEEG19.1.33

Gallagher, A. J., Rutter, H. K., Buckley, D. K., & Molyneux, I. (2012). Lithostratigraphic controls on recharge to the Chalk aquifer of Southern England. *Quarterly Journal of Engineering Geology and Hydrogeology*, *45*(2), 161–172. https://doi.org/10.1144/1470-9236/09-048

Glover, P. W. J. (2009). What is the cementation exponent? A new interpretation. *The Leading Edge*, *28*(1), 82–85. https://doi.org/10.1190/1.3064150

Gulamali, M. Y., Leinov, E., & Jackson, M. D. (2011). Self-potential anomalies induced by water injection into hydrocarbon reservoirs. *Geophysics*, *76*(4), F283–F292. https://doi.org/10.1190/1.3596010

Hunter, R. J. (1981). *Zeta potential in colloid science: Principles and applications*. London: Academic Press Ltd.

Ijioma, A., & Jackson, M. (2014). Closed-loop feedback control of smart wells for production optimization using downhole measurements of self-potential. SPE Annual Technical Conference and Exhibition, Society of Petroleum Engineers.

Ireson, A. M., Mathias, S. A., Wheater, H. S., Butler, A. P., & Finch, J. (2009). A model for flow in the chalk unsaturated zone incorporating progressive weathering. *Journal of Hydrology*, *365*(3–4), 244–260. https://doi.org/10.1016/j.jhydrol.2008.11.043

Jaafar, M. Z., Vinogradov, J., & Jackson, M. D. (2009). Measurement of streaming potential coupling coefficient in sandstones saturated with high salinity NaCl brine. *Geophysical Research Letters*, *36*, L21306. https://doi.org/10.1029/2009GL040549

Jackson, M. D. (2015). Tools and techniques: Self-potential methods. In G. Schubert (Ed.), *Treatise on geophysics* (2nd ed., Vol. 11, pp. 261–293). Amsterdam: Elsevier.

Jackson, M. D., Butler, A. P., & Vinogradov, J. (2012). Measurements of spontaneous potential in chalk with application to aquifer characterization in the southern UK. *Quarterly Journal of Engineering Geology and Hydrogeology*, *45*(4), 457–471. https://doi.org/10.1144/qjegh2011-021

Jackson, M. D., Gulamali, M. Y., Leinov, E., Saunders, J. H., & Vinogradov, J. (2012). Spontaneous potentials in hydrocarbon reservoirs during Waterflooding: Application to water-front monitoring. *SPE Journal*, *17*(01), 53–69. https://doi.org/10.2118/135146-PA

Jacob, C. E. (1950). Flow of ground water. In H. Rouse (Ed.), *Engineering hydraulics* (pp. 321–386). New York: John Wiley.

Jones, H. K., & Robins, N. S. (Eds) (1999). *The Chalk aquifer of the South Downs*, *Hydrogeological Report Series of the British Geological Survey*, Keyworth, Nottingham: British Geological Survey.

Jougnot, D., Linde, N., Haarderb, E. B., & Looms, M. C. (2015). Monitoring of saline tracer movement with vertically distributed self-potential measurements at the HOBE agricultural test site, Voulund, Denmark. *Journal of Hydrology*, *521*, 314–327. https://doi.org/10.1016/j.jhydrol.2014.11.041

Jouniaux, L., Maineult, A., Naudet, V., Pessel, M., & Sailhac, P. (2009). Review of self-potential methods in hydrogeophysics. *Comptes Rendus Geoscience*, *341*(10–11), 928–936. https://doi.org/10.1016/j.crte.2009.08.008

Konikow, L. F. (2011). The secret to successful solute-transport modeling. *Ground Water*, *49*(2), 144–159. https://doi.org/10.1111/j.1745-6584.2010.00764.x

Lanteri, Y., Fievet, P., & Szymczyk, A. (2009). Evaluation of the steric, electric, and dielectric exclusion model on the basis of salt rejection rate and membrane potential measurements. *Journal of Colloid and Interface Science*, *331*(1), 148–155. https://doi.org/10.1016/j.jcis.2008.11.014

Leinov, E., & Jackson, M. D. (2014). Experimental measurements of the SP response to concentration and temperature gradients in sandstones with application to subsurface geophysical monitoring. *Journal of Geophysical Research - Solid Earth*, *119*, 6855–6876. https://doi.org/10.1002/2014JB011249

Limbrick, K. J. (2002). Estimating daily recharge to the Chalk aquifer of southern England—A simple methodology. *Hydrology and Earth System Sciences*, *6*(3), 485–496. https://doi.org/10.5194/hess-6-485-2002

MacAllister, D. (2016). Monitoring seawater intrusion into the fractured UK chalk aquifer using measurements of self-potential (SP). Department of Earth Science and Engineering, Imperial College London, PhD Thesis, 258 pp.

MacAllister, D. J., Jackson, M. D., Butler, A. P., & Vinogradov, J. (2016). Tidal influence on self-potential measurements. *Journal of Geophysical Research - Solid Earth*, *121*, 8432–8452. https://doi.org/10.1002/2016JB013376

MacAllister, D. J., Jackson, M. D., Butler, A. P., & Vinogradov, J. (2018). Remote detection of saline intrusion in a coastal aquifer using borehole measurements of self-potential. *Water Resources Research*, *54*, 1669–1687. https://doi.org/10.1002/2017WR021034

MacDonald, A. M., & Allen, D. J. (2001). Aquifer properties of the Chalk of England. *Quarterly Journal of Engineering Geology and Hydrogeology*, *34*(4), 371–384. https://doi.org/10.1144/qjegh.34.4.371

Maineult, A., Strobach, E., & Renner, J. (2008). Self-potential signals induced by periodic pumping tests. *Journal of Geophysical Research*, *113*, B01203. https://doi.org/10.1029/2007JB005193

Martínez-Pagán, P., Jardani, A., Revil, A., & Haas, A. (2010). Self-potential monitoring of a salt plume. *Geophysics*, *75*(4), Wa17–Wa25. https://doi.org/10.1190/1.3475533

Mathias, S. A. (2005). Modelling flow and transport in the Chalk unsaturated zone. Department of Civil and Environmental Engineering, Imperial College London, PhD Thesis, 195 pp.

McDonald, R. J., Russill, N. R. W., Miliorizos, M., & Thomas, J. W. (1998). In N. S. Robins (Ed.), *A geophysical investigation of saline intrusion and geological structure beneath areas of tidal coastal wetland at Langstone Harbour, Hampshire, UK* (Vol. 130, pp. 77–94). London: Special Publications, Groundwater Pollution, Aquifer Recharge and Vulnerability, Geological Society.

Molyneux, I. (2012). *Hydrogeological characterisation of the Chalk: With specific reference to unsaturated zone behaviour*. Brighton: University of Brighton.

Morgan, L. K., & Werner, A. D. (2015). A national inventory of seawater intrusion vulnerability for Australia. *Journal of hydrology regional studies*, *4*, 686–698. https://doi.org/10.1016/j.ejrh.2015.10.005

MWH (2006). Drought management—Deployable output water quality assessments of critical sources in Sussex: Balsdean desk study. Report prepared for Southern Water Ltd.Final Report No. 41512744.

Nelson, P. H. (2009). Pore-throat sizes in sandstones, tight sandstones, and shales. *AAPG Bulletin*, *93*(3), 329–340. https://doi.org/10.1306/10240808059

Perrier, F. E., Petiau, G., Clerc, G., Bogorodsky, V., Erkul, E., Jouniaux, L., et al. (1997). A one-year systematic study of electrodes for long period measurements of the electric field in geophysical environments. *Journal of Geomagnetism and Geoelectricity*, *49*(11), 1677–1696. https://doi.org/10.5636/jgg.49.1677

Price, M. (1987). Fluid flow in the Chalk of England. In J. C. Goff, & B. P. J. Williams (Eds.), *Fluid flow in sedimentary basins and aquifers, 34* (pp. 141–156). London: Geological Society.

Revil, A. (1999). Ionic diffusivity, electrical conductivity, membrane and thermoelectric potentials in colloids and granular porous media: A unified model. *Journal of Colloid and Interface Science*, *212*(2), 503–522. https://doi.org/10.1006/jcis.1998.6077

Revil, A., & Linde, N. (2006). Chemico-electromechanical coupling in microporous media. *Journal of Colloid and Interface Science*, *302*(2), 682–694. https://doi.org/10.1016/j.jcis.2006.06.051

Revil, A., & Linde, N. (2011). Comment on 'Streaming potential dependence on water-content in Fontainebleau sand' by V. Allègre, L. Jouniaux, F. Lehmann and P. Sailhac. *Geophysical Journal International*, *186*(1), 113–114. https://doi.org/10.1111/j.1365-246X.2010.04850.x

Revil, A., Pezard, P. A., & Glover, P. W. J. (1999). Streaming potential in porous media. 1. Theory of the zeta potential. *Journal of Geophysical Research*, *104*(B9), 20021–20031. https://doi.org/10.1029/1999JB900089

Roubinet, D., Irving, J., & Pezard, P. A. (2018). Relating topological and electrical properties of fractured porous media: Insights into the characterization of rock fracturing. *Minerals*, *8*(1). https://doi.org/10.3390/min8010014

Sandberg, S. K., Slater, L. D., & Versteeg, R. (2002). An integrated geophysical investigation of the hydrogeology of an anisotropic unconfined aquifer. *Journal of Hydrology*, *267*(3–4), 227–243. https://doi.org/10.1016/S0022-1694(02)00153-1

Saunders, J. H., Jackson, M. D., & Pain, C. C. (2008). Fluid flow monitoring in oilfields using downhole measurements of electrokinetic potential. *Geophysics*, *73*(5), E165–E180. https://doi.org/10.1190/1.2959139

Savitsky, A., & Golay, M. J. E. (1964). Smoothing and differentiation of data by simplified least squares procedures. *Analytical Chemistry*, *36*(8), 1627–1639. https://doi.org/10.1021/ac60214a047

Schurch, M., & Buckley, D. (2002). Integrating geophysical and hydrochemical borehole-log measurements to characterize the Chalk aquifer, Berkshire, United Kingdom. *Hydrogeology Journal*, *10*(6), 610–627.

Shi, L., & Jiao, J. J. (2014). Seawater intrusion and coastal aquifer management in China: A review. *Environmental Earth Sciences*, *72*(8), 2811–2819. https://doi.org/10.1007/s12665-014-3186-9

Sill, W. R. (1983). Self-potential modeling from primary flows. *Geophysics*, *48*(1), 76–86. https://doi.org/10.1190/1.1441409

Simmons, C. T., Bauer-Gottwein, P., Graf, T., Kinzelbach, W., Kooi, H., Li, L., et al. (2010). *Variable density groundwater flow: From modelling to applications*. Cambridge: Cambridge University Press.

Small, C., & Nicholls, R. J. (2003). A global analysis of human settlement in coastal zones. *Journal of Coastal Research*, *19*, 584–599.

Soley, R. W. N., Power, T., Mortimore, R. N., Shaw, P., Dottridge, J., Bryan, G., & Colley, I. (2012). In M. G. Shepley, et al. (Eds.), *Modelling the hydrogeology and managed aquifer system of the Chalk across southern England* (Vol. 364, pp. 129–154). London: Groundwater Resources Modelling: A Case Study from the UK, Geological Society.

Steyl, G., & Dennis, I. (2010). Review of coastal-area aquifers in Africa. *Hydrogeology Journal*, *18*(1), 217–225. https://doi.org/10.1007/s10040-009-0545-9

Telford, W. M., Geldart, L. P., & Sheriff, R. E. (1990). *Applied geophysics* (2nd ed.). UK: Cambridge University Press. https://doi.org/10.1017/CBO9781139167932

Vinogradov, J., Jaafar, M. Z., & Jackson, M. D. (2010). Measurement of streaming potential coupling coefficient in sandstones saturated with natural and artificial brines at high salinity. *Journal of Geophysical Research*, *115*, B12204. https://doi.org/10.1029/2010JB007593

Voss, C. I., & Provost, A. M. (2002). SUTRA: A model for saturated-unsaturated variable-density ground-water flow with solute or energy transport. U.S. Geological Survey Water-Resources Investigations Report. 02-4231: 291.

Walton, N. R. G. (1989). Electrical-conductivity and Total dissolved solids—What is their precise relationship. *Desalination*, *72*(3), 275–292. https://doi.org/10.1016/0011-9164(89)80012-8

Wellings, S. R. (1984). Recharge of the upper Chalk Aquifer at a site in Hampshire, England.1. Water-balance and unsaturated flow. *Journal of Hydrology*, *69*(1–4), 259–273. https://doi.org/10.1016/0022-1694(84)90166-5

Werner, A. D., Bakker, M., Post, V. E. A., Vandenbohede, A., Lu, C. H., Ataie-Ashtiani, B., et al. (2013). Seawater intrusion processes, investigation and management: Recent advances and future challenges. *Advances in Water Resources*, *51*, 3–26. https://doi.org/10.1016/j.advwatres.2012.03.004

Westermann-Clark, G. B., & Christoforou, C. C. (1986). The exclusion-diffusion potential in charged porous membranes. *Journal of Electroanalytical Chemistry*, *198*(2), 19.

Williams, A., Bloomfield, J., Griffiths, K., & Butler, A. (2006). Characterising the vertical variations in hydraulic conductivity within the Chalk aquifer. *Journal of Hydrology*, *330*(1–2), 53–62. https://doi.org/10.1016/j.jhydrol.2006.04.036

Winston, R. B. (2014). Modifications made to ModelMuse to add support for the Saturated-Unsaturated Transport model (SUTRA). (ed.), U.S. Geological Survey Techniques and Methods, book 6.

WWAP United Nations World Water Assessment Programme (2014). *United Nations World Water Development Report 2014*. Paris: United Nations World Water Assessment ProgrammeWater and Energy.

Zaidman, M. D., Middleton, R. T., West, L. J., & Binley, A. M. (1999). Geophysical investigation of unsaturated zone transport in the Chalk in Yorkshire. *Quarterly Journal of Engineering Geology*, *32*(2), 185–198. https://doi.org/10.1144/GSL.QJEG.1999.032.P2.08